Scale Effects in a Distributed SWE and Snowmelt Model for Mountain Basins

Don Cline
National Operational Hydrologic Remote Sensing Center
Office of Hydrology, National Weather Service, NOAA

Kelly Elder
Department of Earth Resources
Colorado State University

Roger Bales
Department of Hydrology and Water Resources
University of Arizona

1.0 Abstract.

We present results of an investigation into the effect of increasing spatial and temporal resolutions on modeled distributions of SWE and snowmelt in the Emerald Lake Watershed of the Sierra Nevada of California, U.S.A. We used a coupled remote sensing/distributed energy balance snowmelt model (SNODIS), and used previously validated results from a high spatial (30-m) and temporal (hourly) resolution model run in ELW as a control. We selected spatial resolutions that are commensurate with standard product DEMs or with existing or planned satellite remote sensing data, and temporal resolutions that are factors of typical operational intervals for meteorological data. We degraded the spatial resolution of the DEM from 30 m to 90, 250, and 500 m prior to computing the distributed micrometeorological data. We degraded the classified remote sensing data to the same spatial resolutions prior to computing the duration of the snowcover. Similarly, we degraded the temporal resolution of the micrometeorological data from 1 hour to 3 and 6 hours prior to computing the distributed energy balance and snowmelt. We compared mean basin SWE, basin snowpack water volume, and the spatial patterns of SWE from each test to our previous, high-resolution results. We found no significant differences between the mean basin-wide SWE computed from the 250-m and 500-m spatial resolutions and that of our high-resolution control, regardless of temporal resolution. At each temporal resolution mean basin SWE was over-estimated at the 90-m resolution by 14-17%. Coarsening of the spatial resolution did result in a loss of explicit information regarding the location of SWE in the basin, as expected. We discuss these results in terms of their implications for applying the SNODIS model to larger regions.

2.0 Introduction

Although the importance of water stored in mountain snowpacks is widely recognized, we lack adequate methods of assessing the magnitude of this resource and forecasting its release over time. Simple empirical techniques have been used operationally to estimate the volume of snowmelt runoff for over forty years with reasonable success, but they generally provide little information about the timing or rate of snowmelt runoff. A major limitation of such empirical techniques is their dependence on boundary conditions governing the development of calibration parameters. This dependence may cause such methods to fail in extreme or unusual years, which often are the years of particular interest. In the calibration phase of conceptual snowmelt-runoff models, parameters are typically optimized to produce good fits between observed and simulated streamflow. Since many factors influence streamflow besides SWE and snowmelt characteristics, such models are forced to accommodate a variety of possible biases built into the model parameters. This can result in false compensation of incorrect estimates of SWE and snowmelt by model parameters related to other processes. A third limitation common to most empirical SWE and snowmelt models a dependence on a small number of ground SWE observations within a basin of interest, and the degree to which those observations may or may not be representative of the snowpack conditions elsewhere in the basin.These examples are but some of the many problems and difficulties associated with current operational snowpack assessment and snowmelt-runoff forecasting techniques.

To help address these problems, we developed a physically based, spatially distributed model to estimate the spatial distribution of SWE and snowmelt in mountain basins (SNODIS) [*Cline, Bales, and Dozier*, 1997]. The SNODIS model couples remotely sensed snow cover duration information with a spatial energy balance model to back-calculate, at the end of a snowmelt season, the distribution of SWE at peak accumulation and the distribution of snowmelt through the season. The SNODIS model is based on the simple conceptual idea that the duration of snowcover during the ablation season at a particular location is a function of 1) the amount of SWE at that location at the beginning of the ablation season, and 2) the energy available to melt the snow through the course of the season. SNODIS uses a time series of remotely sensed imagery to determine the duration of snow cover on every pixel, and uses a spatial energy balance model to determine how much energy is available to melt snow over time. Shortwave and longwave radiation exchanges, and turbulent energy exchanges are modeled at every pixel. The SNODIS model provides an estimate of the distribution of SWE without ground observations of SWE or discharge measurements. Thus it provides an independent, physically based estimate of the distribution of SWE and snowmelt that could be used to improve estimates of water resources stored in mountain snowpacks, to improve estimates of the timing, rate, and magnitude of snowmelt runoff, and to provide SWE information to assist calibration of operational conceptual snowmelt-runoff models.

Our initial test of the SNODIS model was at the Emerald Lake Watershed (ELW) in the Sierra Nevada of California [*Cline, Bales, and Dozier*, 1997]. We tested SNODIS under conditions of high spatial (30-m) and high temporal (hourly) resolutions. We found that under these conditions SNODIS produced an estimate of the magnitude and distribution of SWE at peak accumulation that compared well with results from previous methods,

snow course data, and to models of SWE based on field measurements. We statistically compared the mean and variance of the SNODIS-modeled SWE distribution to 180 snow course measurements in the basin [*Melack, et al.*, 1996] and found no significant differences. We compared the modeled spatial patterns of SWE to measured patterns from previous years [*Elder, Dozier, and Michaelson*, 1991], and found only small differences that would be expected from interannual variations in SWE distributions. We compared the SNODIS-modeled total basin SWE volume to results from a binary regression tree SWE distribution model that is based on field measurements, and that had been successfully developed and tested in the same basin (SWETREE) [*Elder*, 1995; *Elder, Michaelson, and Dozier*, 1995]. The total basin water volume stored as snow agreed within 1% between the two methods. Based on these initial successful results and the physical nature of the model, we concluded that SNODIS should be applicable over larger mountain regions.

As a first step towards extending the SNODIS model to larger regions, this paper evaluates the effects of increasing spatial and temporal resolutions on distributions of SWE and snowmelt modeled by SNODIS. Larger resolutions would be desirable for regional-scale modeling principally to reduce computational and data requirements, particularly for operational applications. We tested spatial resolutions that are commensurate with standard product DEMs or with existing or planned satellite remote sensing data, and temporal resolutions that are factors of typical operational intervals for meteorological data. The successful results under high-resolution conditions permit us to treat the original model run as a control against which we can compare new model runs that test conditions of coarser spatial and temporal resolutions.

3.0 Methods

We used the original, high-resolution (30-m spatial resolution, hourly temporal resolution) SNODIS results for the 1993 water year at ELW [*Cline, Bales, and Dozier*, 1997] as a control against which to compare results of this sensitivity study. ELW is a small (120 ha) high alpine basin in Sequoia National Park, Sierra Nevada, California (Figure 1). *Tonnessen* [1991] describes the watershed in detail. In the original high-resolution study, we mapped fractional (sub-pixel) snowcover at three dates using Landsat TM and the spectral unmixing algorithm of *Rosenthal and Dozier* [1996]. We modeled hourly incident solar radiation using a two-stream radiative transfer model for rugged terrain (TOPORAD) [*Dozier and Frew*, 1990]. We extrapolated hourly air temperature, relative humidity, and wind speed across the basin from a micrometeorological instrument site located near the outlet of the basin using a 30-m DEM. We modeled incident longwave radiation as a function of the previously extrapolated air temperature and relative humidity using the Idso2 formulation (*Idso*, 1981]. We considered the energy balance of the snowpack each hour at each pixel as

$$\Delta Q_S + \Delta Q_M = K^* + L^* + Q_E + Q_H + Q_G + Q_R \qquad \text{(EQ 1)}$$

where ΔQ_S is the convergence or divergence of sensible heat fluxes within the snowpack volume, ΔQ_M is the change in latent heat due to melting or freezing, K* is the net shortwave radiation flux, L* is the net longwave radiation flux, Q_H is the sensible heat flux, Q_E

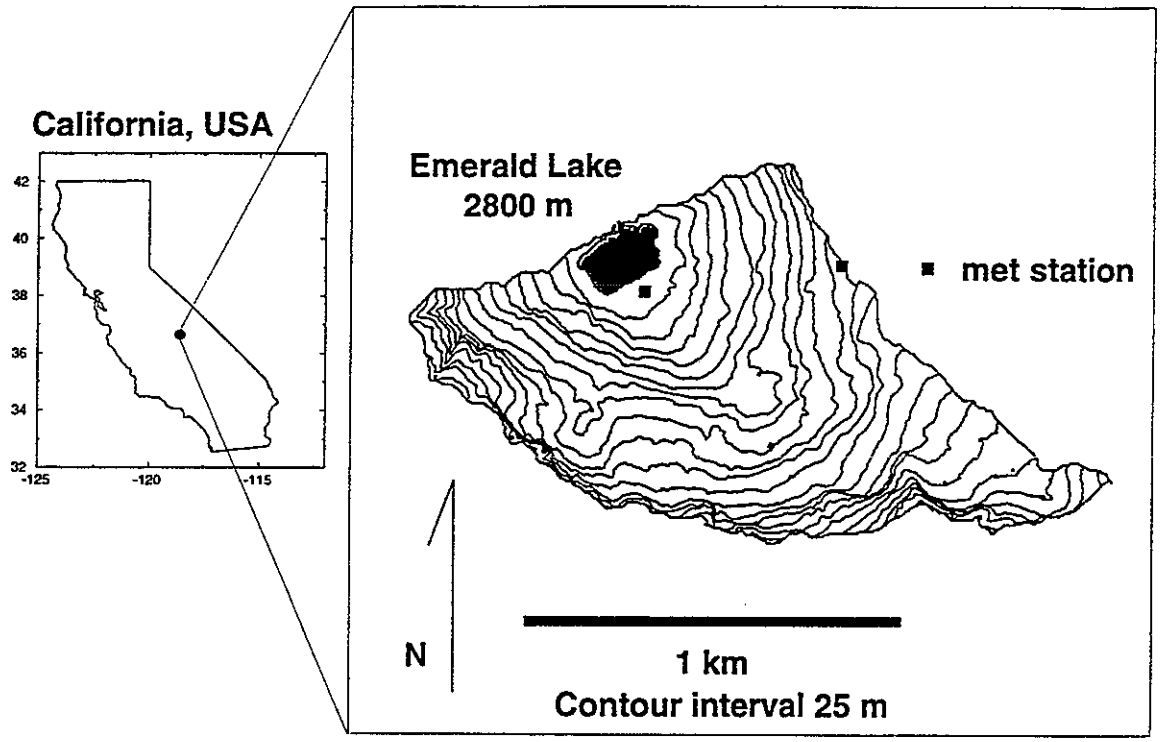

FIGURE 1. Map showing Emerald Lake watershed study area.

is the latent heat flux, Q_G is the ground heat flux, and Q_R is the heat advected by precipitation. If the snowpack is below 0°C, changes in the residual energy term $\Delta Q_S+\Delta Q_M$ result in a temperature change within the snowpack. If the snowpack is at 0°C, net energy losses will cool the snowpack while net energy gains will result in snowmelt. We considered the ground heat flux to be negligible, and precipitation recorded during the modeling period was also negligible. We modeled the turbulent fluxes using the bulk aerodynamic algorithms in SNTHERM89.rev4 [*Jordan*, 1991]. To solve the terms on the right side of EQ. 1 we made assumptions concerning the change of albedo over time, snow surface temperatures, snow emissivities, and the roughness length of the snowpack [*Cline, Bales, and Dozier*, 1997]. We computed a running total of the residual energy term ΔQS+ΔQM for each pixel to provide a value for the total energy available to melt snow at each time step. At the time of each remote sensing scene, the total energy for snowmelt at each pixel was weighted by the fractional area of the pixel that had become snow-free since the previous remote sensing date, and converted to mass units to determine the amount of SWE that would have existed on that fraction of the pixel at the beginning of the model run.

In this study we duplicated the methodology used by *Cline, Bales, and Dozier* [1997] with the exception that we systematically modified the spatial and temporal resolutions of the data used in the model to perform a series of sensitivity tests. We degraded the spatial resolution of the DEM from 30 m to 90, 250, and 500 m using a nearest-neighbor algorithm prior to computing the distributed micrometeorological data (Figure 2). This approach mimics a surface sampling approach commonly used in photogrammetric DEM

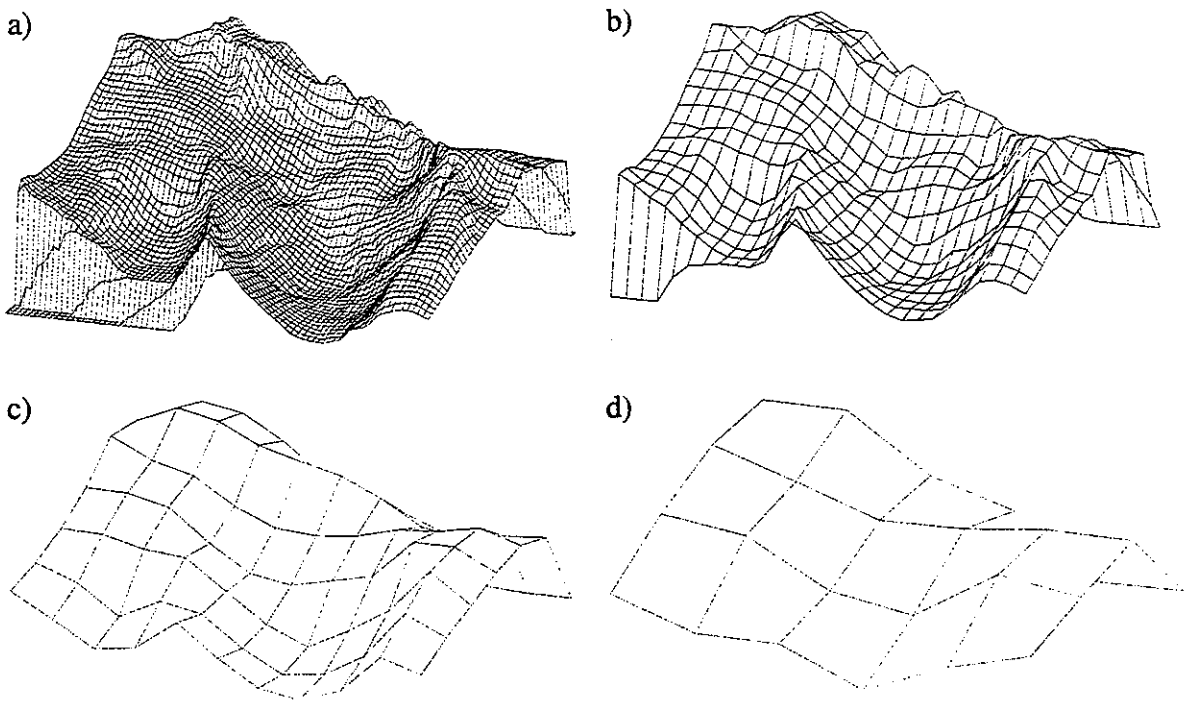

FIGURE 2. Views of degraded DEM data: a) 30-m resolution, b) 90-m, c) 250-m, and d) 500 m. The views are looking from the north-northwest to the south-southeast.

production. We degraded the classified remote sensing data to the same spatial resolutions prior to computing the duration of the snowcover. Since these data lie in a range from 0 to 1, a spatial averaging algorithm was used which resulted in the new, larger pixels having a fractional snowcovered area equal to the sum of the snowcovered areas of the smaller component pixels. We degraded the temporal resolution of the micrometeorological data from 1 hour to 3 and 6 hours prior to computing the distributed energy balance and snowmelt. We simply discarded the unneeded observations, retaining every third or every sixth observation (beginning at midnight) accordingly. Since the recording and averaging formats and intervals of meteorological data are variable, we considered this method of degrading the temporal resolution representative of the crudest data likely to be used.

We completed a total of nine tests, estimating the distribution of SWE and snowmelt for each paired combination of 90, 250, and 500 spatial resolutions and 1, 3, and 6 hour temporal resolutions. For each test, we compared the mean basin SWE ($\overline{SWE}$), the total basin volume of SWE, the spatial pattern of SWE, and modeled snowmelt to the results from the 30-m, hourly control test described above.

4.0 Results

4.1 Mean and Variance of Estimated Basin SWE

Summary statistics describing the test estimates of SWE are shown in Table 1. All tests resulted in a reduction in the range of estimated SWE values within the basin; the lower values were particularly affected. Two-tailed t-tests were performed for each test to deter-

TABLE 1. Summary statistics of basin-wide SWE for the control and each test.

Spatial Resolution (m)	Temporal Resolution (hr)	$\overline{SWE}$ (m)	Percent Difference (%)	Standard Deviation (m)	Minimum SWE (m)	Maximum SWE (m)
30	1	2.13	---	0.54	0.20	3.80
90	1	2.50	+ 17.0	0.30	1.29	3.56
90	3	2.43	+14.2	0.29	1.28	3.44
90	6	2.42	+13.6	0.29	1.21	3.55
250	1	2.18	-0.7	0.21	1.54	2.37
250	3	2.06	-3.4	0.21	1.51	2.30
250	6	2.07	-3.0	0.23	1.47	2.34
500	1	2.03	-4.6	0.29	1.59	2.31
500	3	1.97	-7.5	0.28	1.54	2.24
500	6	2.10	-1.5	0.30	1.62	2.43

mine whether the test $\overline{SWE}$ was significantly different from the control $\overline{SWE}$ of 2.13 m (H_o: $\overline{SWE}_{test} = 2.13$ m, 5% significance level). The null hypothesis was rejected in the three tests at 90-m spatial resolution, indicating that the estimated means of 2.42-2.52 m were statistically different from the control. All the remaining tests failed to reject the null hypothesis. Therefore at 250-m and 500-m spatial resolutions, for all three temporal resolutions, the model estimated the correct $\overline{SWE}$. F-tests were performed to determine whether the variance of basin SWE (σ^2_{swe}) of each test was significantly different from the variance of the control of 0.029 m^2 (Ho: $\sigma^2_{swe} = (0.54\ m)^2$, 5% significance level). The null hypothesis was rejected in all cases except the three at 500-m spatial resolution. At 500-m resolution, the degrees of freedom in the F-tests were substantially reduced from the other cases, permitting a larger value of $F_{critical}$. Nonetheless, the F-tests suggest that the variance of estimated basin SWE was the same at the 500-m spatial resolution as at the 30-m resolution.

4.2 Total Basin Water Volume Stored as SWE

The estimated total volume of water stored as SWE in the basin from each test was computed by summing the volume on each pixel within the basin, and is compared to the control value in Table 2. Changes to the raster depiction of the basin boundaries at coarser spatial resolutions resulted in larger estimates of the basin area at the coarser spatial reso-

lutions. As a result, the estimated total basin SWE volume was affected. Note that the esti-

TABLE 2. Comparison of estimated total basin SWE volume to control.

Spatial Resolution (m)	Temporal Resolution (hr)	Total Basin SWE Volume (m^3)	Difference (m^3)	Percent Difference (%)	Basin Area (m^2)	Corrected SWE Volume (m^3)
30	1	2,740,000	---	---	1,286,100	2,740,000
90	1	3,255,100	+515,100	+18.7	1,304,100	3,210,170
90	3	3,174,192	+434,192	+ 15.8	1,304,100	3,130,380
90	6	3,158,543	+418,543	+15.3	1,304,100	3,114,947
250	1	3,308,790	+568,790	+20.8	1,562,500	2,723,484
250	3	3,216,719	+476,719	+17.4	1,562,500	2,647,694
250	6	3,231,047	+491,047	+17.9	1,562,500	2,659,487
500	1	3,049,870	+309,870	+11.3	1,500,000	2,614,962
500	3	2,956,935	+216,935	+7.9	1,500,000	2,535,276
500	6	3,150,750	+410,750	+15.0	1,500,000	2,701,453

mated total basin SWE volume normalized by the basin area for the respective spatial resolution is equal to the $\overline{SWE}$ shown in Table 1. Thus the apparent over-estimation of the total basin SWE volume in each of the tests is solely an artifact of the raster delineation of basin boundaries in those cases where the estimated $\overline{SWE}$ was less than the control. When the SWE volumes are corrected by normalizing for the high-resolution basin area (Table 2), the problem is corrected for the tests at 250-m and 500-m. These results are shown to illustrate this potential problem that could be encountered when modeling at regional scales. In this case, the problem could be easily corrected by using a vector basin boundary delineation to determine the total basin SWE volume.

4.3 Comparison of Spatial Patterns of SWE

Coarsening the spatial resolution of the model resulted in increasing losses of information about the location of SWE in the basin (Figure 3). To facilitate comparison, the results shown here are standardized to zero mean and unit variance so that each image is displayed with the same grayscale. At each spatial resolution, changes in temporal resolution had only negligible effects on the spatial patterns of SWE, so are not shown here. The 30-m control image (Figure 3a) shows areas of low SWE on the steep ridge forming the southern and western boundary of the basin (A1, 2), on the ridge forming the extreme northeast boundary of the basin (A3), and on steep cliff bands midway up the basin (A4). Areas of large SWE include flatter areas at the base of steep slopes (A5), on the valley floor (A6), in a protected area in the upper reaches of the watershed (A7), and on a broad bench on the western side of the basin (A8).

At 90-m resolution (Figure 3b), the areas of low SWE are still located along the steep ridges (B1), but to a lesser extent, and on some of the cliff areas in the lower part of the basin (B2). The smaller areas of low SWE in the control, such as on the intermediate cliff bands, are not estimated at this resolution. Areas of large SWE include the protected

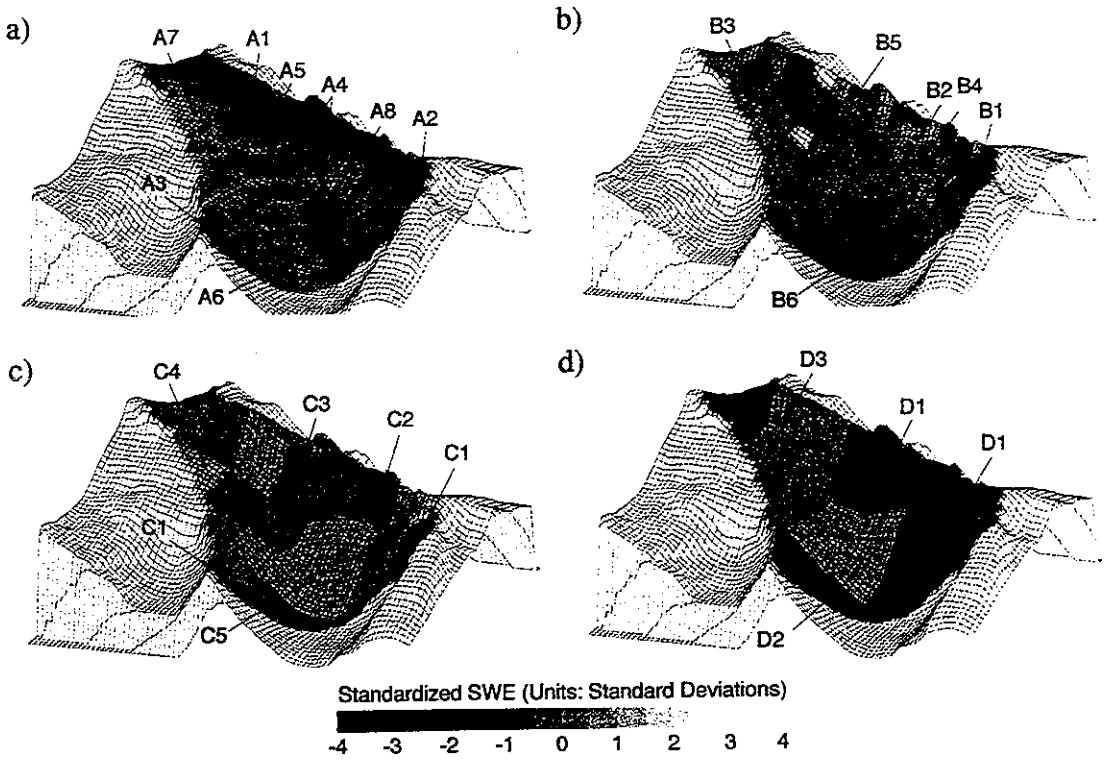

FIGURE 3. Modeled SWE distributions at a) 30-m resolution (control), b) 90 m, c) 250 m, and d) 250 m. These results are for the 1-hr temporal resolution; differences between these patterns and the patterns for the 3-hr adn 6-hr resolutions are negligible. Results are standardized to zero mean and unit variance to facilitate comparison; the grayscale shown is in units of standard deviations away from the mean. The key labels are described in the text.

region in the upper reaches of the basin (B3) and the broad bench on the western side of the basin (B4). SWE is overestimated on the ridge top itself (B5). Here slopes are flatter in the 90-m model, and as a result are estimated to receive more solar radiation. With more apparent energy available during the same period of time, the model estimates greater SWE. SWE is underestimated on the valley floor (B6).

At 250-m resolution (Figure 3c), areas of lowest SWE remain on the extreme northeast and west ridges (C1), and to a lesser extent along the southeast ridge (C2). At this resolution the model estimates less-than-average SWE across the mid-elevations of the basin (C3), in roughly the same location as the low-SWE areas on the cliff bands in the control image. The protected area in the upper reaches of the basin still are estimated to contain larger amounts of SWE (C4), and large SWE values are estimated on the valley floor (C5). With respect to the lower amounts of SWE in the vicinity of the cliff bands and the increased SWE on the valley floor, the results of the 250-m resolution model more closely resemble the control than the 90-m results.

At 500-m resolution (Figure 3d), the depiction of SWE only crudely resembles the control image. Low SWE areas correctly include the western and southeastern ridges, but because of the large grid scale these low-SWE areas are extended too far downslope into areas of the basin that should contain larger SWE amounts (D1). Areas of larger SWE correctly include the valley floor (D2), such as it is depicted at 500-m, and the protected area in the upper reaches of the basin (D3).

4.4 Effect of Spatial and Temporal Resolution on Modeled Snowmelt

The correct estimation of SWE implicitly suggests that snowmelt modeled at each pixel from the energy balance is correct, but it is possible that compensating errors over the course of the snowmelt season could produce the same result. To simplify evaluation of distributed snowmelt modeled at the coarser spatial and temporal resolutions, we computed the basin-wide hourly energy balance, converted these hourly totals to mass units, and normalized the results to a common basin area of 1,286,100 m^2 of the control (Figure 4). The coarser temporal resolutions clearly result in poorer representations of the diurnal snowmelt cycle, although the modeled snowmelt values generally follow the control values at all spatial and temporal resolutions. Hourly root mean squared errors (RMSE) for

TABLE 3. RMSE of modeled hourly snowmelt compared to control.

1-hr Tests		3-hr Tests		6-hr Tests	
Spatial Resolution	**RMSE (m^3 hr^{-1})**	**Spatial Resolution**	**RMSE (m^3 hr^{-1})**	**Spatial Resolution**	**RMSE (m^3 hr^{-1})**
90 m	716	90 m	1393	90 m	2315
250 m	608	250 m	1343	250 m	2134
500 m	620	500 m	1389	500 m	2122
Mean:	648	**Mean:**	1375	**Mean:**	2190

snowmelt are roughly equivalent at each spatial resolution, but increase with increasing temporal resolutions (Table 3). This is apparent in Figure 4, where the longer time steps result in greater departures from the control values, especially during the morning.

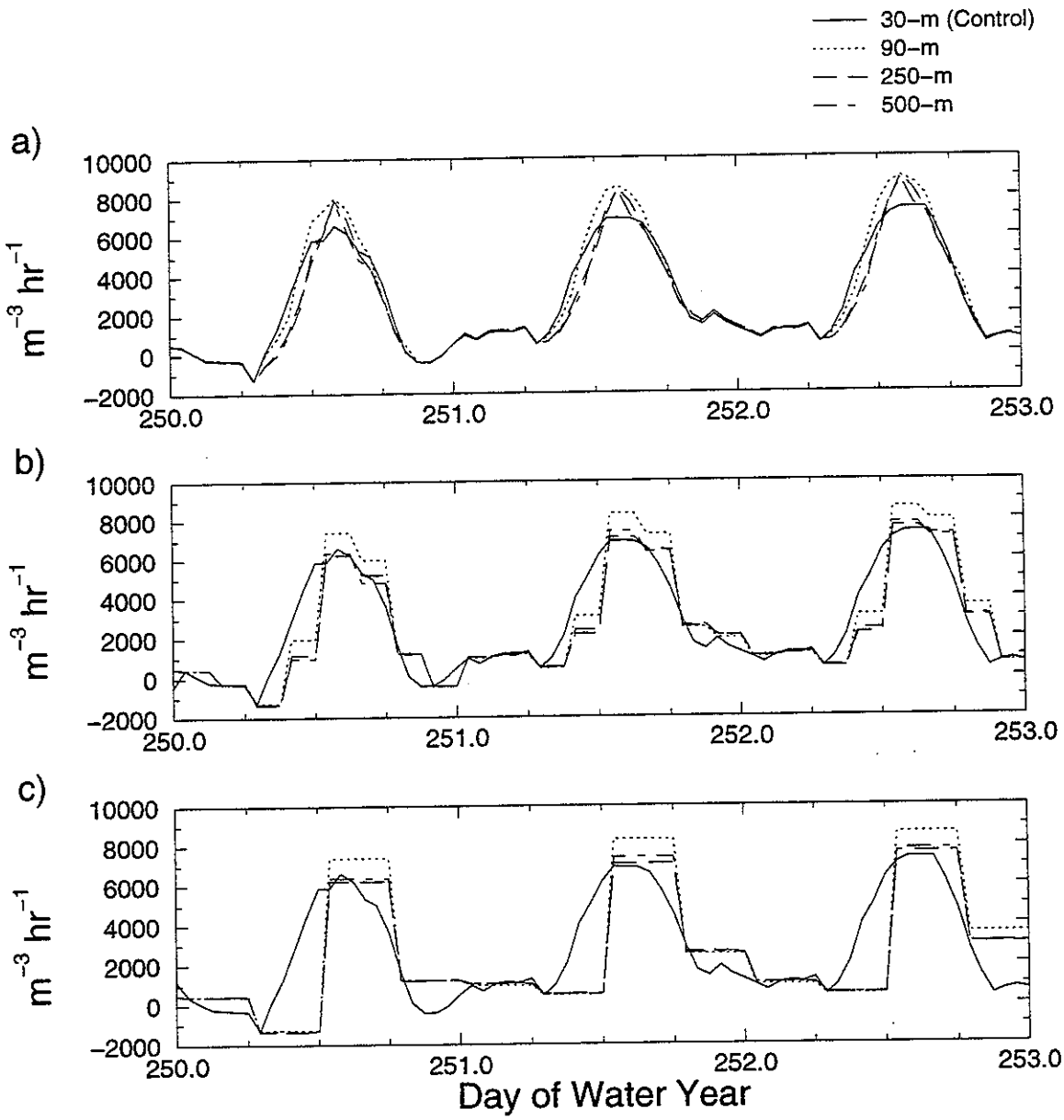

FIGURE 4. Examples of three days of modeled snowmelt at a) 1-hr temporal resolution, b) 3-hr, and c) 6-hr. The control values are shown in each plot for comparison.

5.0 Discussion and Conclusions

The evidence from the sensitivity analysis presented here strongly indicates that the distribution of SWE and snowmelt can be rigorously estimated using the SNODIS model at spatial and temporal scales conducive to regional-scale modeling. If the objective is to

determine the total volume of SWE contained in a basin, reasonable results should be expected using 500-m and 6-hour resolutions. If details of the diurnal timing of snowmelt are required, the 6-hour data may be too crude, at least as far as the degradation method we used here is concerned. Averages, or shorter time steps would be warranted in that case. It is important to realize that the ELW test basin is very small, and contains a limited distribution of topographic characteristics, most notably aspect. The small basin size becomes a concern at the larger spatial resolutions tested, such as the 500-m resolution where only six grid cells depict the basin. Therefore we view these results as an encouraging proof-of-concept, but see a need to test the SNODIS model in a similar fashion over a larger test area. In addition to the study area size, other questions were raised during this study that pertain to the application of this approach over large regions.

Of particular interest is why $\overline{SWE}$ was overestimated at the 90-m resolution but correctly estimated at the larger resolutions. The 90-m resolution results were statistically different from the control mean, although the differences were perhaps not unreasonably large at 14-17%. Increasing the spatial resolution tended to reduce the elevations of the peaks along the southern and eastern ridges of the basin, effectively smoothing the sharp ridge to varying degrees (e.g. Figure 2). Some of the steeper, northerly-facing slopes were reduced as a result, which tended to increase the modeled insolation on these areas. This would tend to increase estimated SWE in the SNODIS methodology. However, this effect occurred at each of the larger spatial resolutions, and the least of this effect was observed in the 90-m case. It is possible that the differences between the 90-m tests and the others are simply a result of the particular coincidence of slopes, aspects, elevations, and snow cover duration that resulted from the spatial resampling to each resolution. Further evaluation of this possibility will require tests to be performed in a larger study area exhibiting a greater range of topographic characteristics. A second possible explanation is a hypothesis that somewhere between 90-m and 250-m a scale threshold exists, below which representation of explicit spatial patterns of the relevant variables strongly matters, and beyond which the explicit distribution of the governing variables becomes relatively unimportant. This would be consistent with the representative elementary area (REA) concept presented by *Wood et al.* [1988] for catchment-scale storm response modeling. Although our scale sensitivity tests employed a different spatial aggregation approach from theirs, fundamentally our tests represent a similar shift from modeling (snowmelt) processes using explicit spatial detail to modeling them using statistical distributions. If such an REA for snowmelt processes exists, it may actually be preferable to apply the SNODIS model at larger regions using coarser resolution governing data. We cannot conclude the existence of an REA for snowmelt modeling from testing only four spatial resolutions. Additional investigation, again preferably in a test basin with a broader range of conditions, will be necessary in order to address this hypothesis.

Our method of resampling the sub-pixel fractional snow cover products ensured that the same amount of snow covered area existed in the larger pixels as in the total of the incorporated smaller pixels. This effectively synthesized a sub-pixel snow fraction product a spectral mixture model snow classification scheme might produce from a coarser resolution sensor. The 250-m and 500-m test resolutions correspond to product resolutions that will be available on the MODIS sensor, planned for launch on the EOS AM-1 spacecraft in June, 1998. The MODIS data should support the determination of sub-pixel snow cover

mapping. An assumption in the SNODIS modeling approach that we did not address here is that the gradual reduction in snow cover fraction over time represents a patch of snow becoming smaller but otherwise not changing locations within a pixel. This assumption seems reasonable for small pixels, such as the 30-m or even the 90-m resolutions, but it may become questionable for larger pixel sizes. The assumption apparently was sufficient in these tests, but further analysis is warranted before presuming that larger resolution remote sensing data will be suitable for driving SNODIS.

6.0 Acknowledgements

This research was supported in part by an Interdisciplinary grant under NASA's Earth Observing System program, and in part by grant EAR-9304933 from the National Science Foundation

7.0 References

Cline, D., R. Bales, and J. Dozier, Estimating the spatial distribution of snow in mountain basins using remote sensing and energy balance modeling, *Water Resources Research*, submitted February 1997.

Elder, K., *Snow Distribution in Alpine Watersheds*, Ph.D. Dissertation, University of California, Santa Barbara, 1995.

Elder, K., J. Dozier, and J. Michaelson, Snow accumulation and distribution in an alpine watershed, *Water Resources Research*, 27, 1541-1552, 1991.

Elder, K., J. Michaelson, and J. Dozier, Small basin modeling of snow water equivalence using binary regression tree methods, in *Biogeochemistry of Seasonally Snow-Covered Catchments*, edited by K.A. Tonnessen, M.W. Williams, and M. Tranter, *IAHS Publ. 228*, 129-139, 1995.

Idso, S.B., A set of equations for full spectrum and 8-14 μm and 10.5-12.5 μm thermal radiation from cloudless skies, *Water Resources Research*, 17, 295-304, 1981.

Jordan, R., A one-dimensional temperature model for a snow cover, *Special Report 91-6*, U.S. Army Cold Regions Research and Engineering Laboratory, Hanover, 1991.

Melack, J.M., J. Sickman, A. Leydecker, and D. Marrett, Comparative analyses of high-altitude lakes and catchments in the Sierra Nevada: Susceptibility to acidification, Final Report to the California Air Resources Board, Contract A032-188, 1996.

Rosenthal, W., and J. Dozier, Automated mapping of montane snow cover at sub-pixel resolution from Landsat Thematic Mapper, *Water Resources Research*, 32(1), 115-130, 1996.

Wood, E.F., M. Sivapalan, K.J. Beven, and L. Band, Effects of spatial variability and scale with implications to hydrologic modeling, *Journal of Hydrology*, 102, 29-47, 1988.